

Machine-learning based high-bandwidth magnetic sensing

Galya Haim,^{1,2} Stefano Martina,^{3,4} John Howell,⁵ Nir Bar-Gill,^{1,5} and Filippo Caruso^{3,4,6}

(galya.haim@mail.huji.ac.il, stefano.martina@unifi.it,

john.howell@mail.huji.ac.il, bargill@phys.huji.ac.il, filippo.caruso@unifi.it)

¹*Institute of Applied Physics, Hebrew University, Jerusalem 91904, Israel*

²*School of Physics, The University of Melbourne, Parkville, Victoria 3010, Australia*

³*Dept. of Physics and Astronomy, University of Florence,
via Sansone 1, I-50019 Sesto Fiorentino (FI), Italy*

⁴*European Laboratory for Non-Linear Spectroscopy (LENs),*

University of Florence, via N. Carrara 1, I-50019 Sesto Fiorentino (FI), Italy.

⁵*Racah Institute of Physics, Hebrew University, Jerusalem 91904, Israel*

⁶*Istituto Nazionale di Ottica del Consiglio Nazionale delle Ricerche (CNR-INO), I-50019 Sesto Fiorentino (FI), Italy*

Recent years have seen significant growth of quantum technologies, and specifically quantum sensing, both in terms of the capabilities of advanced platforms and their applications. One of the leading platforms in this context is nitrogen-vacancy (NV) color centers in diamond, providing versatile, high-sensitivity, and high-resolution magnetic sensing. Nevertheless, current schemes for spin resonance magnetic sensing (as applied by NV quantum sensing) suffer from tradeoffs associated with sensitivity, dynamic range, and bandwidth. Here we address this issue, and implement machine learning tools to enhance NV magnetic sensing in terms of the sensitivity/bandwidth tradeoff in large dynamic range scenarios. We experimentally demonstrate this new approach, reaching an improvement in the relevant figure of merit by a factor of up to 5. Our results promote quantum machine learning protocols for sensing applications towards more feasible and efficient quantum technologies.

Over the past decade, quantum technologies have emerged as an important platform relevant for a broad range of fields, such as quantum communications and quantum sensing. These advances have been driven by the development of experimental realizations exhibiting needed and useful properties.

In the context of quantum sensing, one of the leading systems is based on Nitrogen Vacancy (NV) color centers in diamond [1], which provides a versatile platform for diverse quantum sensing, notably magnetic sensing [2–6]. NVs have found important applications in magnetic sensing, covering paleomagnetometry [7], biosensing [8–11], nuclear magnetic resonance [12–14] and more.

Quantum sensing with NVs is realized through spin resonance measurements, usually detected optically. While this approach achieves quantitative vectorial information with high sensitivity and spatial resolution, it suffers from a trade-off between sensitivity and bandwidth, specifically in the high dynamic range regime. In fact, working with small fields (small dynamic range) enables an optimal sensing strategy, which relies on precise measurements at a predetermined high-sensitivity point (the point of maximal signal gradient). However, this is not possible in the regime of large dynamic range signals.

In this paper, we address this limitation and introduce a Machine Learning (ML) algorithm that significantly improves this trade-off. We demonstrate that training an appropriate neural network using a combination of real and simulated data enables a clear improvement in measurement bandwidth for a given sensitivity goal, in the large dynamic range scenario.

Neural Networks are powerful ML models constituted by interconnected layers of artificial neurons that are

trained to minimize a loss function [15, 16]. Such models have been already used for sensing of magnetic fields and for noise spectroscopy with NV centers [17–19]. By contrast, in this work neural networks find application in the full reconstruction of an external magnetic field. We analyze the network’s performance for a decreasing number of measurement points, while exploring different training dataset sizes, and altering noise and lineshape conditions. We compare these results to similar analysis done for raster scans and find that the network has advantages over raster scanning. With the right training, the network can be insensitive to variations in noise and lineshape. Moreover, the network’s measurement error is more robust and scales better for fewer data points.

As shown in Fig. 1, the standard approach to quantitatively measure vectorial magnetic fields using NVs is essentially a common spin resonance measurement termed Electron Spin Resonance (ESR), usually performed through optical readout for NVs, referred to as Optically Detected Magnetic Resonance (ODMR), using an experimental setup schematically depicted in Fig. 1a [2, 3].

The NV defect orientation within the crystal lattice (Fig. 1b) and its energy level structure (Fig. 1c), enable the optical detection of the NV spin resonances, realized through the combined application of green light excitation and microwave (MW) irradiation, while detecting the NV spin-dependent red fluorescence. As depicted in Fig. 1d, a full ESR spectrum of an NV ensemble consists of eight resonances, representing two resonant frequencies for each one of the four crystallographic orientations the NV can take in a single crystal diamond sample (Fig. 1b). Basically, this measurement amounts to identifying res-

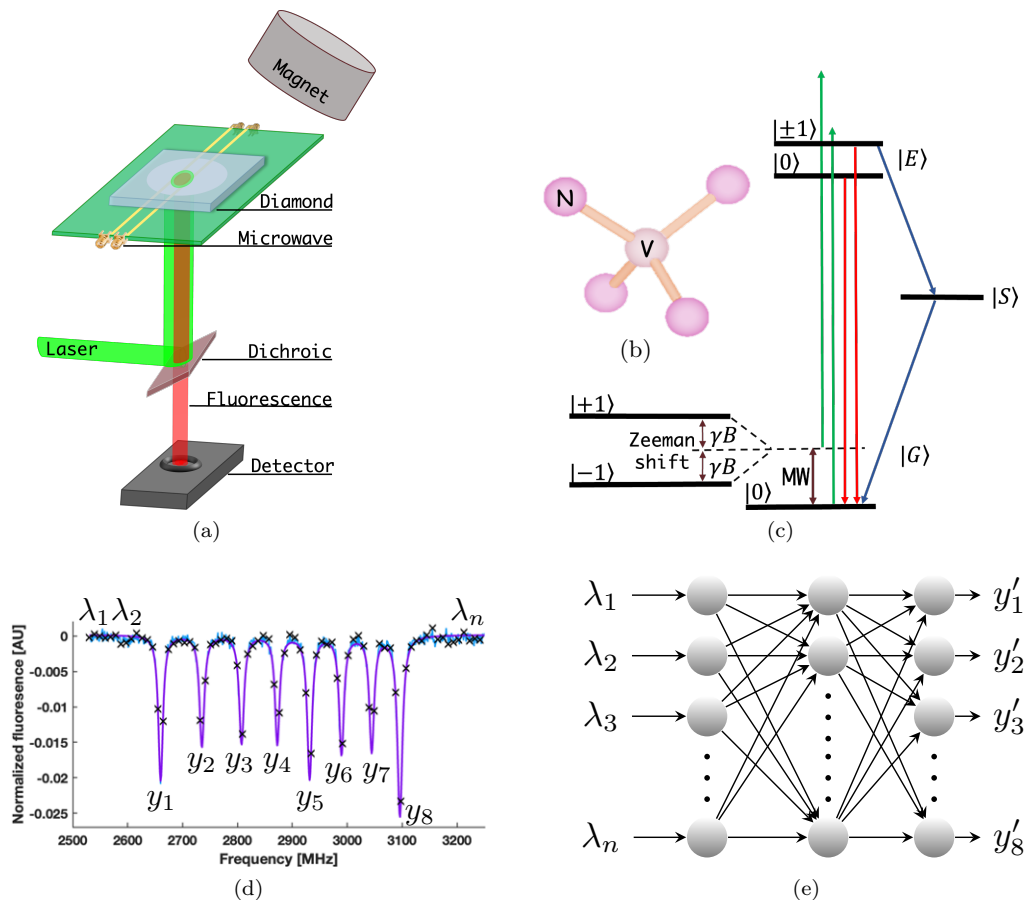


FIG. 1. (a) Experimental setup schematic; MW pulses are used to find the spin resonances of the NV center within the diamond sample related to the external magnetic field orientation and intensity, green excitation laser illuminates the diamond and fluorescence from the NV centers is collected and read by a detector. (b) The NV can appear in four possible orientations within the diamond lattice. (c) NV energy level schematic: triplet ground state; under an external magnetic field the degeneracy between the $m_s = \pm 1$ energy levels is lifted. MW drives transitions between $m_s = 0$ and $m_s = \pm 1$. Excitation of the ground state with Green laser (532 nm) can decay in two ways: one is non-radiative and non-spin conserving through the singlet state. The second path is spin-conserving and radiates in red (650-800 nm). The $m_s = 0$ state decays mostly radiatively, while $m_s = \pm 1$ includes a significant non-radiative decay through the singlet state into the ground spin state $m_s = 0$. (d) ESR spectrum, with measured data in blue and the corresponding fit in purple (to a set of eight Lorentzian functions). In black, a subset of the data, i.e. λ_i . The resonance frequencies are marked with y_i . (e) Schematic of the neural network, the inputs λ_i are the measured data points and the outputs are the predictions y'_i of the eight resonance frequencies y_i .

onance positions (i.e. y_i) in the frequency space. Once obtained, a full vectorial magnetic field can be extracted. Further details regarding the NV system, the experimental setup (Figs. 1a and 1c) and the ODMR measurement scheme can be found in Sec. III.

This process of identifying the resonance positions requires scanning the signal over frequency space (sometimes referred to as raster scanning). This scan should cover the entire relevant frequency range (determined by the desired dynamic range), and the scan resolution (number of data points within the frequency window) is determined by the resonance widths and Signal to Noise Ratio (SNR). There is a minimal scan resolution required to successfully retrieve the resonance frequencies, and in general the measurement error depends on these various parameters (linewidth, SNR, scan resolution), as detailed

in Sec. III.

The sensitivity for an ODMR measurement is defined to be $\eta = (\delta\nu * \sqrt{T})/\gamma$, where $\delta\nu$ is the error for the resonance frequency, T is the measurement time (essentially corresponding to the averaging time and affecting the SNR) and γ is the gyromagnetic ratio of the NV [20]. A shorter measurement time both improves sensitivity and allows for faster measurements, which could be crucial for time varying signals. Reducing measurement time could be achieved by improving the experimental setup, i.e. having higher SNR or better NV properties. However, it is not less important to consider the optimal number of data points in a measurement, as it essentially scales linearly with measurement time.

ML is a research field that deals with the development of artificial intelligence methods that learn from

data. Several approaches were developed to solve the two main supervised ML tasks of classification, i.e. to predict a categorical value associated to some predictors (called features in the ML jargon), and regression where the predicted value is continuous [21]. Supervised learning means that the model is trained to learn to predict based on a ground truth associated to each input. By contrast, in unsupervised learning the dataset is composed only by features without any desired output [21]. In the latter, the main task is called clustering where the model learns to divide the data into groups based on the elements distance. The third ML approach is called reinforcement learning [22] where the model is represented by an agent that learns to implement a policy to decide actions in a simulated environment. Some of the most common classical methods are K-Means for clustering, K-Nearest Neighbor (KNN), decision trees, Support Vector Machine (SVM) and logistic regression for classification tasks and linear regression for regression tasks [21, 23]. Neural Networks were inspired by early research on brain modeling and successively find application as a ML tool. Recently, with the increment of computational power and the increasing availability of large datasets, they overcome other ML algorithms as a general-purpose tool for either clustering, classification and regression tasks. In fact they are capable of universal function approximation [24] and easily adapt to different scenarios. Moreover, increasing the depth of the network allows the model to learn to extract higher level features from the input, and in this context they are denoted by *deep learning* [15, 16]. There are several neural network based models specialized for specific kinds of data, specifically Convolutional Neural Networks (CNN) [25] for images and Recurrent Neural Networks (RNN) [26] for time series and text. Remarkably, in the latter years we are witnessing the rising of generative models for images with Generative Adversarial Networks (GAN) [27], diffusion models [28–30], and text with Large Language Models (LLM) [31].

Quantum Machine Learning (QML) is a growing research field at the intersection of ML and quantum physics and computing [32, 33]. In general, it deals with different approaches depending on the nature of the analyzed data and of the models used to perform it. Classical ML models can be successfully adopted to process quantum data for instance, with the objective to analyze the noise affecting a quantum device [19, 34, 35] or to control quantum dynamics [36]. QML models can be also implemented on quantum devices to perform tasks on classical data [37] or even on fully quantum environments [38].

In particular, in this work we adopt a classical Multilayer Perceptrons (MLPs) in several supervised regression tasks on quantum data. MLPs are neural network models organized in a feed-forward structure [15, 16, 21] as in Fig. 1e. MLPs are trained via gradient descent to minimize a loss function between the prediction and the desired output. More details on the used models are given in Sec. III B.

In the following, we detail our approach of training the ML models to identify the resonance frequencies, given a limited number of measurement points. We compare this scheme to standard raster scanning, as a function of the number of points, and demonstrate the advantages of the machine learning scheme.

I. RESULTS

A. Setup, simulations and models

Our approach relies on training a machine learning model, with real and simulated data, to enable efficient identification of the resonance frequencies in the measured signal. We employ a relevant MLP model and compare it to regular raster scanning as a function of the number of data points (subsampling).

Ninety six full raster scans were measured in an epillumination wide field setup (see Fig. 1a and Sec. III for details), each one under a different externally applied magnetic field which we measure through standard ODMR (since the different fields lead to different resonance frequencies).

Synthetic data was generated based on a simplified NV Hamiltonian [1] considering the Zeeman shift: magnetic fields at various angles (θ and ϕ , respectively longitudinal and azimuthal, with respect to the diamond surface), were projected on the four NV orientations, determining the resonance frequencies. Resonance widths, contrast, and Gaussian noise were chosen to mimic the line-shape of the measured data, producing full ESR spectra with six or eight Lorentzians, similar to the one depicted in Fig. 1d.

The neural network’s input layer dimension (λ_n in Fig. 1e) is determined by the number of data points in an ESR spectrum and therefore was changed as networks were trained for different subsamplings: starting from the full 600-point spectrum, we subsample by taking every other point, every third point and so on, obtaining at the end spectra with 300 points, 200 points and so on. The output layer always consists of eight values that predict the central frequencies of the eight Lorentzians (y'_i). These predictions are then compared to the values extracted from the full ESR spectrum, which is defined to be the ground truth, and the error is defined to be the averaged absolute value of the differences.

To accomplish a fair comparison, a similar process was performed for raster scans: the resonances extracted from subsampled data (through standard Lorentzian curve fitting) were compared to the ones extracted from the full spectrum, and the error is defined in the same way. It is important to note that the subsampled datasets were compared to the full data from which they were derived, and the error in the full scan (with the maximal number of points) is the fit error.

Some of the simulated data samples had overlapping or partly overlapping Lorentzians, for which the centers

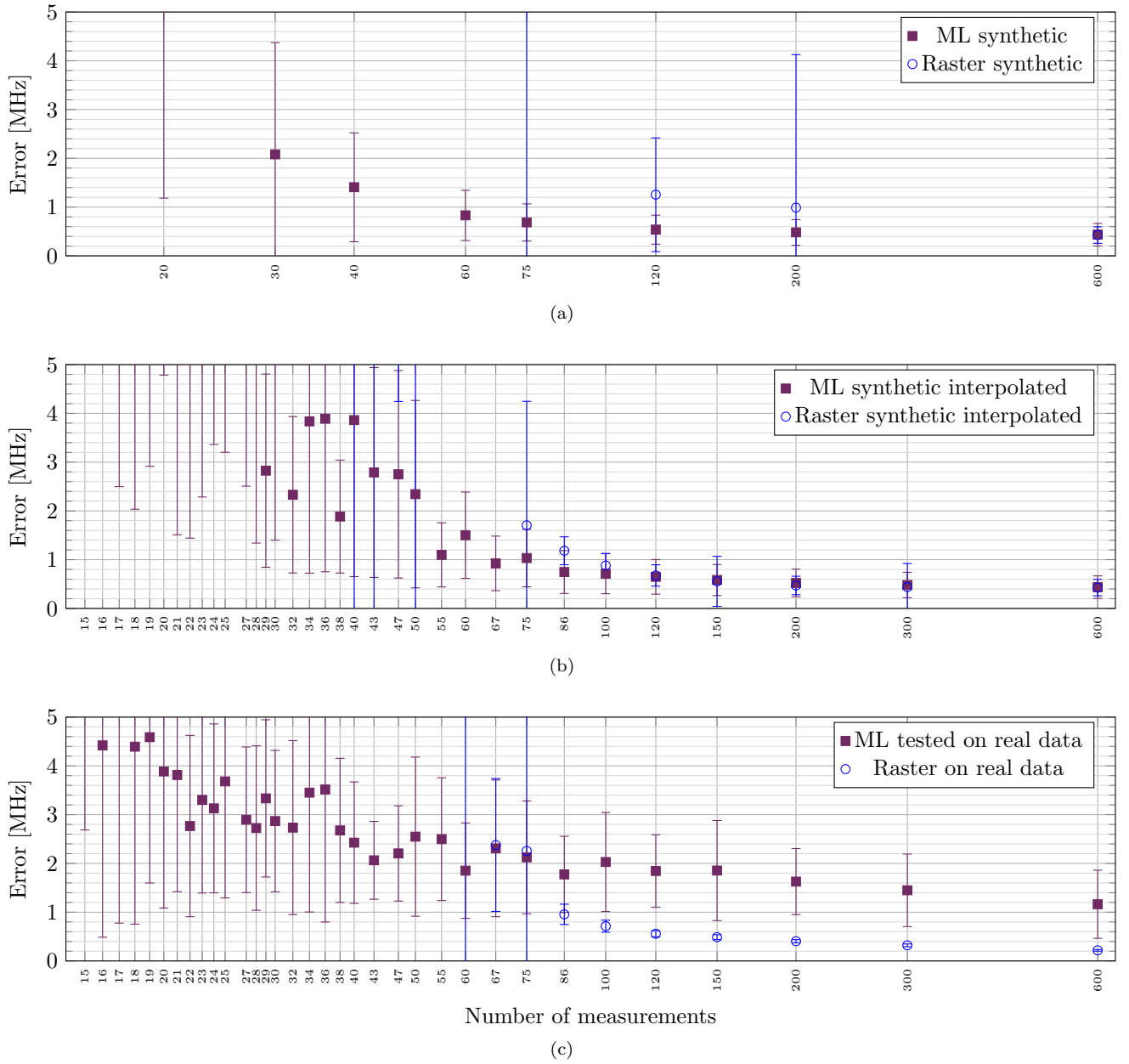


FIG. 2. In (a) and (b), ML networks (purple squares) were trained with 10 000 full-length synthetic samples, validated on 2 000 samples and tested on other 2 000 samples to report the results. The same 2 000 test samples are used to calculate the normalized error of raster scanning (blue circles). In (a) the dataset is subsampled to the specified number of data points and a different network is trained and tested for each subsampling ratio. Accordingly, the raster scan was calculated directly on the subsampled data. In (b) only one network is trained with the 600 data points of the full dataset, then the subsampled data is linearly interpolated to upsample it to the full size for the test. Accordingly, the same procedure is used for the raster scan. (c) Comparison between error of neural networks and normalized error of raster scans for different number of data points. The networks (purple squares) were trained with subsampled datasets, like as the the ones in (a), however, the training dataset contained 1 000 synthetic samples and 50 real data samples, validation was done with 46 real data samples. The same 46 raster were subsampled, the averaged error for those is depicted in blue.

were sometimes too close to be distinguished. Note that for these data samples the neural network still outputs eight values. However, trying to identify eight resonances using a raster scan, especially with lower SNR, would often fail. Raster scans also fail when heavily subsampled,

as one or more of the Lorentzians are no longer recognizable. To account for this statistical trait of the raster scans, we normalize the error by the square root of the success probability, essentially following the definition of the sensitivity and considering the success probability in

terms of time (translating into additional measurements needed, as further explained in Sec. III).

B. Scaling and comparison

Fig. 2a depicts the ML error (purple squares) for networks that were trained with 10 000 samples and validated with 2 000 samples to find the optimal hyperparameters (see Sec. IIIB for details on the model and its hyperparameters). As previously described, here each network was trained on the relevant subsampled data. Blue circles depict the normalized error of subsampled raster scanning, averaged over the same 2 000 samples that were used for the network’s validation. The raster scan error is distinctly high, due to the above-mentioned normalization of the error with the success probability, since in some of the data samples it was not possible to identify 8 Lorentzians. The ML model exhibits better results compared to raster scanning with an error that is more than 400 KHz better (except for the case of full length data), and remarkably, with only 10% of the data points, the ML error is still below 1 MHz. In addition, the ML error has better scaling as a function of the number of data points.

In Fig. 2b we present an alternative training scheme: in this case, just one network was trained and only on a full length dataset (600 frequency points) with 10 000 samples and validated with 2 000 samples. To comply with the structure of the MLP, the network was tested on 2 000 subsampled dataset, that were first linearly interpolated back to full length and, only then, introduced to the network. The averaged error of these is presented in the plot (purple squares). The same 2 000 samples were used to test raster scanning (blue circles), these were also sub-sampled, interpolated and then assessed. The interpolation surprisingly improves the error for raster scanning. In fact, even though it introduces additional noise to the data, the fitting works significantly better, and for a higher number of points, the raster’s error and standard deviation are very similar to the network. However, below 120 data points the ML models shows better results compared to the raster scan. Interpolating data saves on training time, since one network fits all datasets, but at the cost of less favourable performance. In fact, when a model is trained on the full 600-points data, it learns patterns that can be distorted with the subsampling and the subsequent interpolation. For high numbers of points, the two methods are almost equivalent. Although, for lower numbers of points, starting at 120 points, a network trained for the specific number of data points gives a lower averaged error and standard deviation, as can be seen from the comparison of the two graphs in Fig. 2a (and depicted also in Fig. S1b in the supplementary material).

We note that, while not realized here, a hybrid approach might be considered and could be beneficial, wherein several networks could be trained on different

subsampling sizes but not on all of them. In this case, the data to be analyzed could be interpolated to the closest available dimension and the corresponding trained network can be employed for the prediction. This can save training time while keeping the predictions less affected by the effects of the interpolation on the data.

Fig. 2c depicts the result of a network (purple squares) tested on real data, and the subsampling of real raster scans. The networks were trained (as in Fig. 2a) for specific subsamplings, with a combination of 1 000 synthetic data samples along with 50 real data samples, and was tested on 46 real data samples. The same 46 real samples were used to calculate the raster’s normalized error. The raster’s results in Fig. 2c, are better than the previous two, this is mostly due to the fact that in all 46 data samples, the eight Lorentzians were well separated. The network’s error here still has a better scaling than the raster’s error, however, for a high number of points the network error is about 1 MHz worse than the raster, which is in agreement with training predictions that are further explained in the following section.

C. Analysis and generalization

We now turn to a more detailed analysis ML model behavior, further examining the behaviour of the network with regards to other parameters: the size of the training dataset, noise level and Lorentzian widths, which can vary between diamond samples due to coherence properties of the NVs [6].

Fig. 3 depicts the evolution of the validation error during training of the neural network for two dataset sizes: in green, the network was trained with 10 000 simulated samples and validated with 2 000 samples. In red, the network was trained with 1 000 simulated samples and validated with 200 simulated samples. In blue, 50 real data samples were added to the training set, and the validation was performed on 46 real data samples. Even though training with 1 000 samples is not sufficient, as the minimal error is around 2 MHz, there is agreement between the results on synthetic data and the ones on real data. This plot explains the difference between results depicted in Fig. 2c and Fig. 2a - respectively represented here by the blue and green curves, with a difference of 0.5 – 2 MHz between them.

Two important parameters which characterize the resonances measured in ESR experiments are the SNR and the Lorentzian widths. These vary between experimental setups, diamond samples and even individual measurements due to different noise sources. Fig. 4 presents the average error of two networks: in Fig. 4a the network was trained on a simulated dataset in which all 10 000 samples had a width of 10 MHz and subsequently tested on three datasets with 100 data samples, each with different resonance widths: 6 MHz (blue), 10 MHz (green), and 15 MHz (red). When tested on 10 MHz, the network’s averaged error is 0.5 MHz lower than it is for 6 and 15

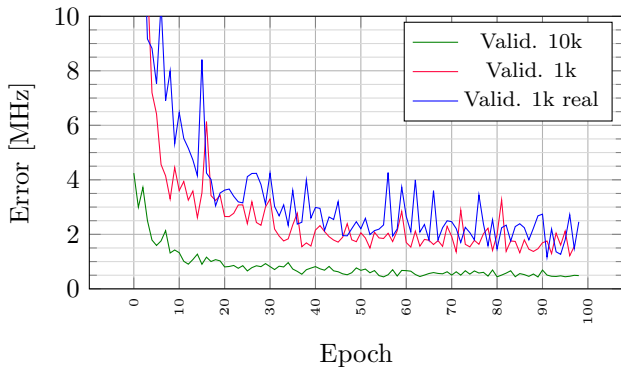


FIG. 3. Evolution of error during the training of ML models, calculated on the validation sets of different datasets. In green (Valid. 10k): training with 10 000 synthetic samples and validated on 2 000 synthetic samples. In red (Valid. 1k): training with 1 000 synthetic samples and validated on 200 synthetic samples. In blue (Valid. 1k real): training with 1 000 synthetic samples plus 50 real samples, validated on 46 different real samples.

MHz. In Fig. 4b the network was trained on a different dataset of 10 000 samples with widths within a range: from 5 MHz to 16 MHz, and then, tested on the same three datasets of Fig. 4a. This way of training proved to be a more robust model, the errors for all the tests are comparable and the network is no longer sensitive to changes in width. Similar behaviour was observed for SNR, Fig. 4c depicts a network that was trained on data samples with SNR of 4, and tested on different samples with SNR 2.5, 4 and 10. Fig. 4d depicts the test results of a network that was trained on samples with SNR randomly sampled within the range [2.5, 10]. Again, the network that was trained on a range is more robust, and when training specifically, the variations show a higher error. The results in Fig. 4 report the averages on 100 test samples, for different number of measurements, using the interpolation training scheme.

Changes in noise and width also have an effect on subsampling raster scans, and are described in detail in Sec. III.

II. DISCUSSION

In this paper we employ ML models to achieve high bandwidth measurements without compromising sensitivity in ESR measurements with NV centers. The neural networks exhibit an advantage over raster scans, it maintains the same error for down to fifth of the data points, while for that sub sampling rate, the raster's error increases by about 800 KHz. The ML models still perform well with an error of less than 1 MHz using only 10% of data points. Moreover, it shows an impressive ability to predict resonance locations in the presence of overlapping Lorentzians. We show the gain and flexibility

of training networks in different ways: interpolating can save on training time while training multiple networks yields a lower error and standard deviation. Furthermore, we show that, for a network to be robust, it needs to be trained on a big enough dataset that is comprised of data in a range of noise and linewidth.

In the regime of sufficient training, we find it useful to have a simulation that well-describes the physics of the NV system, such that the resulting synthetic data is comparable to measured data.

The machine learning techniques applied to this quantum setting prove to be efficient, achieving an improved trade-off between high sensitivity and high dynamic range. They can be adaptively applied to measurements to achieve the desired result. E.g., reducing the measurement time by a factor 5, while maintaining the same error, improves the sensitivity by a factor ~ 2 ; alternatively, the sensitivity can remain constant while reducing the measurement time even further. Such capabilities could have significant impact on a broad range of measurement scenarios with large, time-varying signals, such as characterization of circuit performance, identifying transient biological signals, and more.

III. METHODS

A. Experimental setup and data acquisition

The ground state of NV centers (Fig. 1c) is an effective two-level quantum system. Under green laser excitation, it is possible to initialize the spin to the $m_s = 0$ ground state. In detail, the population occupying $m_s = 0$ would reach the excited state manifold and decay back to the ground state $m_s = 0$, emitting a red photon. The population occupying $m_s = \pm 1$ is more likely to decay through the singlet state, to $m_s = 0$ in a non-radiative way. Within the ground state, spin manipulation is possible with resonant MW pulses, population transfer to $m_s = \pm 1$ would lead to a drop in measured fluorescence.

In the presence of an external magnetic field, degeneracy is lifted off the $m_s = \pm 1$ due to Zeeman shift, the shift is given by γB_{\parallel} , where γ is the gyromagnetic ratio of the NV and B_{\parallel} is the external magnetic field component parallel to the NV axis. In the diamond lattice, there are four possible crystallographic orientations the NV can take (Fig. 1b), and so, in the presence of a magnetic field that is not aligned with any of the orientations, there will be eight resonance frequencies as shown in Fig. 1d, two for each orientation. Once these frequencies are known, the vectorial magnetic field can be calculated.

Ideally, an ESR measurement would have the smallest number of points for which all information about the magnetic field can be obtained from the data, without increasing measurement error, which means lower sensitivity. As can be expected, the error increases as the number of measurement decreases. Below a certain number of measurements, raster scanning is simply not possible as

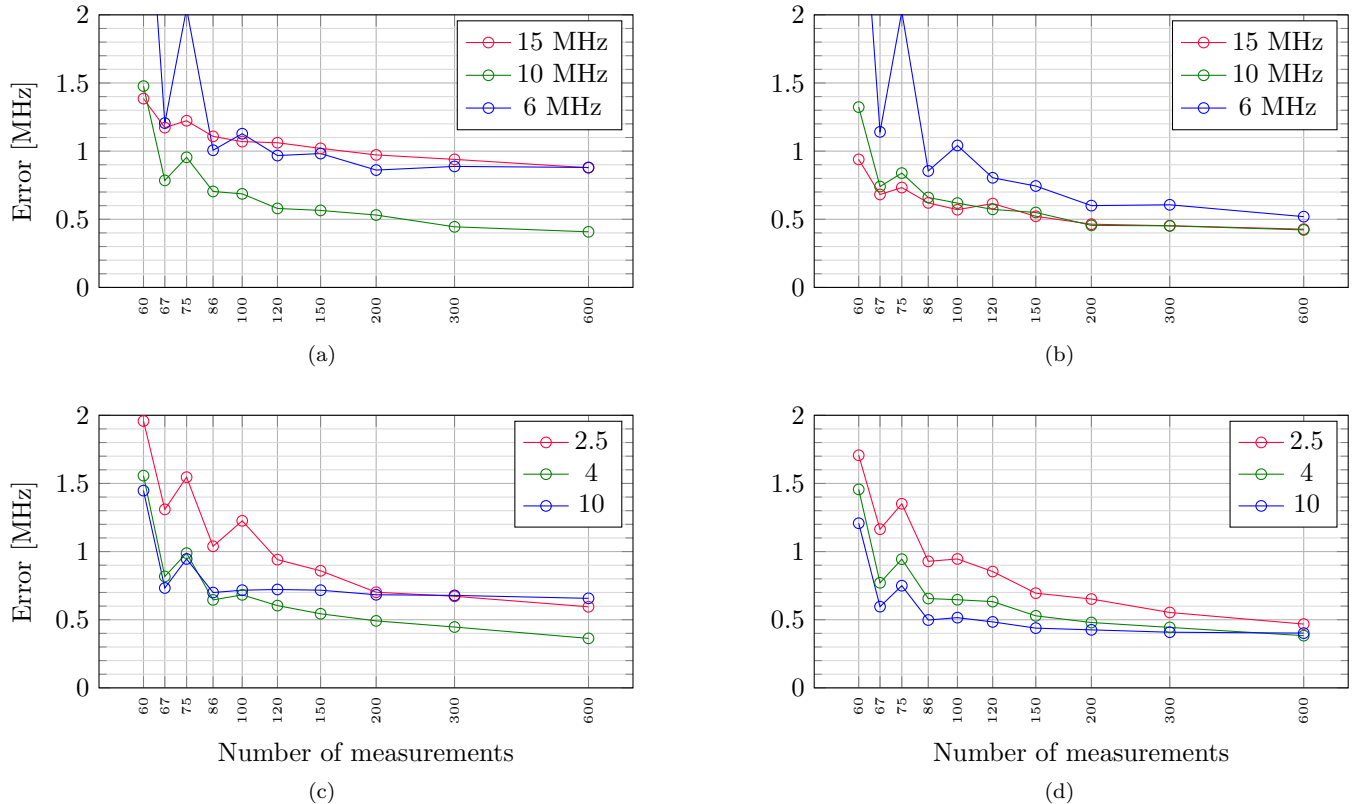


FIG. 4. ML averaged error on simulated data for different number of measurements. All the models are trained on 10 000 samples with 600 data points and tested on different datasets of 100 samples subsampled and successively interpolated to the full dimension. In particular, in (a) the network is trained on samples having 10 MHz Lorentzian width and tested on three different datasets each one having different widths: 6 MHz (blue), 10 MHz (green), and 15 MHz (red). In (b) the network is trained on samples with random width within the range [5, 16] MHz and tested on the same datasets of (a). (c) depicts the averaged error for a model trained on samples with SNR value of 4 and tested on different SNR samples with SNR values of 2.5 (red), 4 (green), and 10 (blue). In (d), the network was trained on samples with random SNR within a range of [2.5, 10] and tested on the same datasets as in (c).

not all eight Lorentzians show in a data sample, this number varies and depends on the measurement bandwidth as well as on SNR. As mentioned in the background, the sensitivity is defined to be $\eta = (\delta\nu * \sqrt{T})/\gamma$. To account for the statistical success of the raster in obtaining eight Lorentzians, We normalize the measurement time, T, by P - the success probability, and so the normalized sensitivity is now $\eta = (\delta\nu * \sqrt{T/P})/\gamma$. Based on that, we define the normalized error to be $\delta\nu/\sqrt{P}$.

Fig. 5 depicts the average error of 100 subsampled simulated raster scans for different SNRs and Lorentzian widths. For a constant noise level (Fig. 5a), error is smaller for narrow Lorentzians. However, the wider Lorentzians can be found for a smaller number of points. For a constant width (Fig. 5b), error increases as SNR decreases.

ESR raster scans were done in an epi-illumination wide field home built microscope. Green laser (lighthouse, Sprout), illuminates the diamond sample through an objective, and fluorescence is collected by an sCMOS camera (Andor Neo). Microwaves are generated by Wind-

freak and delivered to the sample with a custom made Omega shaped waveguide (Fig. 1a).

B. Machine learning model

In this section we give more details on the ML models in Fig. 1e employed to predict the position of the deeps y_i in the ESR spectrum. Specifically, they are MLPs trained with Adam [39] to minimize the Mean Squared Error (MSE) loss between the predictions y'_i and the ground truth y_i given by the spectrum. The dimensions of the input and output layers are defined by the problem and are respectively given by the number of ESR data points $\lambda_1, \dots, \lambda_n$ and the eight deeps positions. The number of layers in the network and their size are treated as hyperparameters to be optimized and, in order to keep the procedure as simple as possible, the tunable number of neurons is the same for every hidden layer. Also, the task is formulated as a regression problem, and all the inputs and outputs are normalized between zero and one

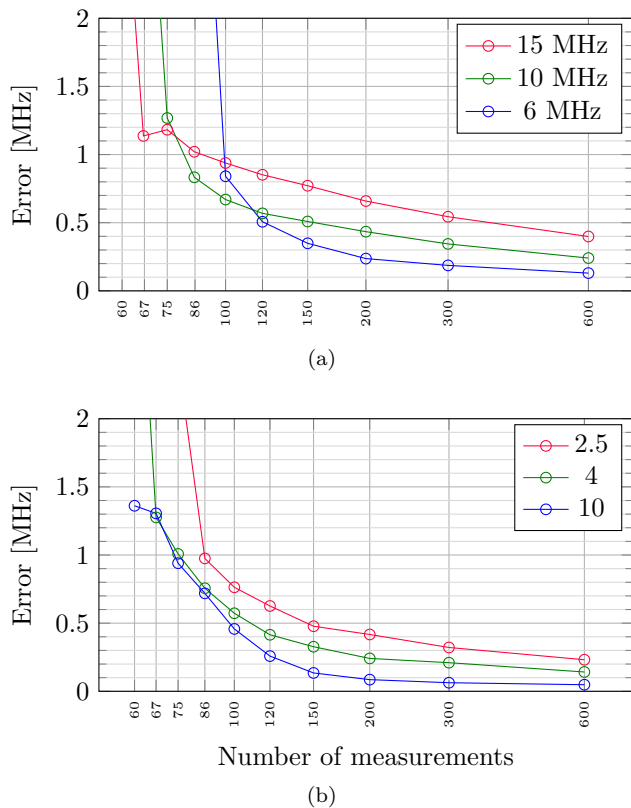


FIG. 5. Raster subsampling error (not normalized) behaviour with respect to the number of measurements, averaged over 100 data samples. In (a), with constant SNR, subsampling rasters with Lorentzian width of 6 (blue), 10 (green) and 15 (red) MHz. In (b), with constant width, subsampling rasters with different SNRs: 10 (blue), 4 (green) and 2.5 (red).

within the data range. The activation functions for all layers are RELU ($\max(0, x)$) except for the sigmoid in the output layer.

In detail, we employ the MLP model that is composed of fully connected layers each one of a certain number of artificial neurons. A single artificial neuron returns the scalar

$$\hat{y} \equiv f(\mathbf{w}^T \cdot \mathbf{x} + b) \quad (1)$$

obtained by applying the non linear function $f: \mathbb{R} \rightarrow \mathbb{R}$ to the weighted sum of the inputs $\mathbf{x} \in \mathbb{R}$ with the weights \mathbf{w} plus the bias term b . Globally, a MLP of L layers is defined by the relation

$$\mathbf{h}_\ell = f_\ell(W_\ell^T \mathbf{h}_{\ell-1} + \mathbf{b}_\ell), \quad (2)$$

for $\ell = 1, \dots, L$, where $\mathbf{h}_\ell \in \mathbb{R}^{k_\ell}$ is the vector of the k_ℓ outputs of the ℓ -th layer of the MLP, $\mathbf{h}_{\ell-1} \in \mathbb{R}^{k_{\ell-1}}$ is the vector of the $k_{\ell-1}$ outputs of the previous layer $\ell - 1$ and $W_\ell \in \mathbb{R}^{k_{\ell-1} \times k_\ell}$ and $\mathbf{b} \in \mathbb{R}^{k_\ell}$ are respectively the weights and biases in matrix form for all the neurons of the layer ℓ . By definition, $\mathbf{h}_0 \equiv \boldsymbol{\lambda}$ are the inputs of the MLP and $\mathbf{h}_L \equiv \mathbf{y}'$ its final outputs. Accordingly, the

layer with the inputs (the layer 0 in eq. (2)) is called the input layer, the last layer L is called the output layer, and all the other layers are called hidden layers. The number of layers L , the number of neurons in each layer k_1, \dots, k_L , and the kind of activation function f_1, \dots, f_L are the hyperparameters that define the structure of the models. The number of neurons of the output layer, k_L is defined by the task and in our case is fixed to eight with sigmoid activation function to predict the frequencies of the Lorentzian y_1, \dots, y_8 in the ESR spectrum. Likewise, the number of inputs are defined by the task and in our case is equal to the number of measurements $\lambda_1, \dots, \lambda_n$ in the ESR spectrum that are 600 for the full raster scan and fractions of it for the subsampled spectra. Regarding the other layers, in our work we decided to keep the number of neurons equal for all layers $k \equiv k_1 = \dots = k_{L-1}$ and all the activation functions f_1, \dots, f_{L-1} are equal to the *relu* function $f = \max(0, x)$. The values of L and k are optimized with a dedicated framework [40] along with other training hyperparameters, specifically the *learning rate*, the *batch size* and the amount of regularization with *dropout* and *weight decay*. The neural networks are trained with *gradient descent* to minimize the error of the predictions \mathbf{y}' respect to the ground truth \mathbf{y} in the form of the MSE loss:

$$\mathcal{L}(\mathbf{y}, \hat{\mathbf{y}}) = \frac{1}{8n} \sum_{i=1}^n \sum_{j=1}^8 (y_{i,j} - \hat{y}_{i,j})^2. \quad (3)$$

A generic gradient descent method aims to find the parameters $\boldsymbol{\theta}$ of the neural network (that is, W_ℓ^T and \mathbf{b}_ℓ in eq. (2) for all ℓ) so that the loss is minimized. The latter is implemented iteratively by calculating

$$\boldsymbol{\theta}_{t+1} = \boldsymbol{\theta}_t - \eta \nabla_{\boldsymbol{\theta}} \mathcal{L}(\mathbf{y}|_{B_t}, \hat{\mathbf{y}}|_{B_t}), \quad (4)$$

where η is the learning rate that determines the step length, $\nabla_{\boldsymbol{\theta}}$ is the gradient of the loss surface in $\boldsymbol{\theta}$ and the notation $\cdot|_{B_t}$ indicates that we use a subset B_t of the training dataset called *minibatch* (whose dimension is determined by the batch size hyperparameter) to calculate the gradients for a single descent step. The entire training dataset is used, iteratively batch by batch, to perform the training steps and a full pass through all the data is called *epoch*. Specifically, we train the models using Adam [39] that implements gradient descent with *adaptive momentum*.

The prediction error for the neural networks is quantified by the Mean Absolute Error (MAE):

$$MAE(\mathbf{y}, \hat{\mathbf{y}}) = \frac{1}{8n} \sum_{i=1}^n \sum_{j=1}^8 |y_{i,j} - \hat{y}_{i,j}|, \quad (5)$$

where $y_{i,j}$ is the ground truth value and $\hat{y}_{i,j}$ is the predicted value for the j -th deep of the i -th sample. Regarding the Lorentzian fitting procedure, we can also integrate the prediction confidence into the error calcula-

tion, thus we define the MAE for that case as:

$$MAE(\mathbf{y}, \hat{\mathbf{y}}, \mathbf{c}) = \frac{1}{8n} \sum_{i=1}^n \sum_{j=1}^8 \sqrt{(y_{i,j} - \hat{y}_{i,j})^2 + c_{i,j}^2}, \quad (6)$$

where $y_{i,j}$ and $\hat{y}_{i,j}$ are the same as before and $c_{i,j}$ is the confidence for the prediction of the j -th deep of the i -th sample.

All models are trained for a maximum of 100 epochs. At the end we keep the parameters for the model that has the minimum MAE error on the validation set and we use it to report the results. The error in the validation set is also used to perform hyperparameter optimization. In general, the hyperparameters affect the number of parameters of the model, and thus its complexity, and how it is trained. The optimization procedure of these hyperparameters consists of searching for the best combination of the values for the number of layers L and their size k in eq. (2), the learning rate η and the size $|B|$ of the mini-batches B_t in eq. (4), and the amount of regularization in the form of dropout and weight decay. The latter two regularization terms represents a way to simplify the model complexity without reducing his parameters. In detail, the dropout consists in randomly disabling with a certain probability the output of neurons within the network [41]. In this way, the reliance on single features represented by single neurons is discouraged during training. The weight decay strategy, also called $L2$ regularization, enforces a penalty term on the loss in order to keep the weights small and therefore constraint the parameters space.

The hyperparameter optimization is implemented using the *Ray Tune* platform [40] adopting a Bayesian technique called *Hyperopt* [42]. The latter uses Tree-structured *Parzen* estimators [43] to suggest the most probable best combination for the hyperparameters, and the distribution is updated at every trial where a model with the proposed combination is trained on

the training set and evaluated on the validation set. Moreover, to speed up the process, we adopted the *ASHA* scheduler [44] to early stop the least promising trials before the end of their training. We considered the following ranges for the hyperparameters to optimize: $L \sim \text{lograndint}(1, 32)$ for the number of layers; $k \sim \text{lograndint}(1, 1024)$ for the size of the layers; $\eta \in \{10^{-2}, 10^{-3}, 10^{-4}\}$ for the learning rate; $|B| \in \{2, 4, 8, 16, 32\}$ for the batch size; the dropout in $\{0, 0.2, 0.5\}$ and the weight decay in $\{0, 10^{-6}, 10^{-5}, 10^{-4}, 10^{-3}\}$.

The codes used for the implementation and training of the neural networks and for the generation of simulated data are available on the GitHub repository: <https://github.com/trianam/machineLearningMagneticSensing>.

ACKNOWLEDGMENTS

This work was financially supported by the European Union’s Horizon 2020 research and innovation programme under FET-OPEN GA No. 828946–PATHOS. G.H. also acknowledges support from the Melbourne research scholarship. S.M. also acknowledges financial support from the PNRR MUR project PE0000023–NQSTI. N.B. and F.C. also acknowledge financial support by the European Commission’s Horizon Europe Framework Programme under the Research and Innovation Action GA No. 101070546–MUQUABIS. N.B. also acknowledges financial support by the Carl Zeiss Stiftung (HYMMS wildcard), the Ministry of Science and Technology, Israel, the innovation authority (Project No. 70033), and the ISF (Grants No. 1380/21 and No. 3597/21). F.C. also acknowledges financial support by the European Defence Agency under the project Q-LAMPS Contract No. B PRJ-RT-989.

-
- [1] M. W. Doherty, F. Dolde, H. Fedder, F. Jelezko, J. Wrachtrup, N. B. Manson, and L. C. L. Hollenberg, Theory of the ground-state spin of the nv^- center in diamond, *Phys. Rev. B* **85**, 205203 (2012).
 - [2] J. M. Taylor, P. Cappellaro, L. Childress, L. Jiang, D. Budker, P. R. Hemmer, A. Yacoby, R. Walsworth, and M. D. Lukin, High-sensitivity diamond magnetometer with nanoscale resolution, *Nature Physics* **4**, 810 (2008).
 - [3] J. R. Maze, P. L. Stanwix, J. S. Hodges, S. Hong, J. M. Taylor, P. Cappellaro, L. Jiang, M. V. G. Dutt, E. Togan, A. S. Zibrov, A. Yacoby, R. L. Walsworth, and M. D. Lukin, Nanoscale magnetic sensing with an individual electronic spin in diamond, *Nature* **455**, 644 (2008).
 - [4] M. S. Grinolds, S. Hong, P. Maletinsky, L. Luan, M. D. Lukin, R. L. Walsworth, and A. Yacoby, Nanoscale magnetic imaging of a single electron spin under ambient conditions, *Nature Physics* **9**, 215 (2013).
 - [5] L. T. Hall, J. H. Cole, C. D. Hill, and L. C. L. Hollenberg, Sensing of fluctuating nanoscale magnetic fields using nitrogen-vacancy centers in diamond, *Phys. Rev. Lett.* **103**, 220802 (2009).
 - [6] J. M. Taylor, P. Cappellaro, L. Childress, L. Jiang, D. Budker, P. R. Hemmer, A. Yacoby, R. Walsworth, and M. D. Lukin, High-sensitivity diamond magnetometer with nanoscale resolution, *Nature Physics* **4**, 810 (2008).
 - [7] E. Farchi, Y. Ebert, D. Farfurnik, G. Haim, R. Shaar, and N. Bar-Gill, Quantitative vectorial magnetic imaging of multi-domain rock forming minerals using nitrogen-vacancy centers in diamond, *Spin* **7**, 1740015 (2017).
 - [8] J. F. Barry, M. J. Turner, J. M. Schloss, D. R. Glenn, Y. Song, M. D. Lukin, H. Park, and R. L. Walsworth, Optical magnetic detection of single-neuron action potentials using quantum defects in diamond, *Proceedings of the National Academy of Sciences* **113**, 14133 (2016), <https://www.pnas.org/doi/pdf/10.1073/pnas.1601513113>.

- [9] Y. Ninio, N. Waiskopf, I. Meirzada, Y. Romach, G. Haim, U. Banin, and N. Bar-Gill, High-sensitivity, high-resolution detection of reactive oxygen species concentration using nv centers, *ACS Photonics* **8**, 1917–1921 (2021).
- [10] J. C. Price, R. Mesquita-Ribeiro, F. Dajas-Bailador, and M. L. Mather, Widefield, spatiotemporal mapping of spontaneous activity of mouse cultured neuronal networks using quantum diamond sensors, *Frontiers in Physics* **8**, 10.3389/fphy.2020.00255 (2020).
- [11] L. P. McGuinness, Y. Yan, A. Stacey, D. A. Simpson, L. T. Hall, D. Maclaurin, S. Prawer, P. Mulvaney, J. Wrachtrup, F. Caruso, R. E. Scholten, and L. C. L. Hollenberg, Quantum measurement and orientation tracking of fluorescent nanodiamonds inside living cells, *Nature Nanotechnology* **6**, 358 (2011).
- [12] H. J. Mamin, M. Kim, M. H. Sherwood, C. T. Rettner, K. Ohno, D. D. Awschalom, and D. Rugar, Nanoscale nuclear magnetic resonance with a nitrogen-vacancy spin sensor, *Science* **339**, 557 (2013), <https://www.science.org/doi/pdf/10.1126/science.1231540>.
- [13] L. M. Pham, S. J. DeVience, F. Casola, I. Lovchinsky, A. O. Sushkov, E. Bersin, J. Lee, E. Urbach, P. Cappellaro, H. Park, A. Yacoby, M. Lukin, and R. L. Walsworth, Nmr technique for determining the depth of shallow nitrogen-vacancy centers in diamond, *Phys. Rev. B* **93**, 045425 (2016).
- [14] C. Müller, X. Kong, J.-M. Cai, K. Melentijević, A. Stacey, M. Markham, D. Twitchen, J. Isoya, S. Pezzagna, J. Meijer, J. F. Du, M. B. Plenio, B. Naydenov, L. P. McGuinness, and F. Jelezko, Nuclear magnetic resonance spectroscopy with single spin sensitivity, *Nature Communications* **5**, 4703 (2014).
- [15] Y. LeCun, Y. Bengio, and G. Hinton, Deep learning, *nature* **521**, 436 (2015).
- [16] I. Goodfellow, Y. Bengio, and A. Courville, *Deep Learning* (MIT Press, 2016) <http://www.deeplearningbook.org>.
- [17] R. Santagati, A. A. Gentile, S. Knauer, S. Schmitt, S. Paesani, C. Granade, N. Wiebe, C. Osterkamp, L. P. McGuinness, J. Wang, M. G. Thompson, J. G. Rarity, F. Jelezko, and A. Laing, Magnetic-field learning using a single electronic spin in diamond with one-photon readout at room temperature, *Phys. Rev. X* **9**, 021019 (2019).
- [18] K. Jung, M. H. Abobeih, J. Yun, G. Kim, H. Oh, A. Henry, T. H. Taminiau, and D. Kim, Deep learning enhanced individual nuclear-spin detection, *npj Quantum Information* **7**, 41 (2021).
- [19] S. Martina, S. Hernández-Gómez, S. Gherardini, F. Caruso, and N. Fabbri, Deep learning enhanced noise spectroscopy of a spin qubit environment, *Machine Learning: Science and Technology* **4**, 02LT01 (2023).
- [20] L. Pham, *Magnetic Field Sensing with Nitrogen-Vacancy Color Centers in Diamond. Doctoral dissertation* (Harvard University, 2013).
- [21] C. M. Bishop and N. M. Nasrabadi, *Pattern recognition and machine learning*, Vol. 4 (Springer, 2006).
- [22] R. S. Sutton and A. G. Barto, *Reinforcement learning: An introduction* (MIT press, 2018).
- [23] T. Hastie, R. Tibshirani, J. H. Friedman, and J. H. Friedman, *The elements of statistical learning: data mining, inference, and prediction*, Vol. 2 (Springer, 2009).
- [24] B. Hanin, Universal function approximation by deep neural nets with bounded width and relu activations, *Mathematics* **7**, 10.3390/math7100992 (2019).
- [25] J. Gu, Z. Wang, J. Kuen, L. Ma, A. Shahroudy, B. Shuai, T. Liu, X. Wang, G. Wang, J. Cai, and T. Chen, Recent advances in convolutional neural networks, *Pattern Recognition* **77**, 354 (2018).
- [26] Y. Yu, X. Si, C. Hu, and J. Zhang, A Review of Recurrent Neural Networks: LSTM Cells and Network Architectures, *Neural Computation* **31**, 1235 (2019), <https://direct.mit.edu/neco/article-pdf/31/7/1235/1053200/neco.a.011199.pdf>.
- [27] I. Goodfellow, J. Pouget-Abadie, M. Mirza, B. Xu, D. Warde-Farley, S. Ozair, A. Courville, and Y. Bengio, Generative adversarial networks, *Commun. ACM* **63**, 139–144 (2020).
- [28] J. Sohl-Dickstein, E. Weiss, N. Maheswaranathan, and S. Ganguli, Deep unsupervised learning using nonequilibrium thermodynamics, in *Proceedings of the 32nd International Conference on Machine Learning*, Proceedings of Machine Learning Research, Vol. 37, edited by F. Bach and D. Blei (PMLR, Lille, France, 2015) pp. 2256–2265.
- [29] J. Ho, A. Jain, and P. Abbeel, Denoising diffusion probabilistic models, in *Advances in Neural Information Processing Systems*, Vol. 33, edited by H. Larochelle, M. Ranzato, R. Hadsell, M. Balcan, and H. Lin (Curran Associates, Inc., 2020) pp. 6840–6851.
- [30] H. Cao, C. Tan, Z. Gao, Y. Xu, G. Chen, P.-A. Heng, and S. Z. Li, A survey on generative diffusion models, *IEEE Transactions on Knowledge and Data Engineering* **36**, 2814 (2024).
- [31] W. X. Zhao, K. Zhou, J. Li, T. Tang, X. Wang, Y. Hou, Y. Min, B. Zhang, J. Zhang, Z. Dong, Y. Du, C. Yang, Y. Chen, Z. Chen, J. Jiang, R. Ren, Y. Li, X. Tang, Z. Liu, P. Liu, J.-Y. Nie, and J.-R. Wen, A survey of large language models (2023), arXiv:2303.18223 [cs.CL].
- [32] I. S. Maria Schuld and F. Petruccione, An introduction to quantum machine learning, *Contemporary Physics* **56**, 172 (2015), <https://doi.org/10.1080/00107514.2014.964942>.
- [33] J. Biamonte, P. Wittek, N. Pancotti, P. Rebentrost, N. Wiebe, and S. Lloyd, Quantum machine learning, *Nature* **549**, 195 (2017).
- [34] S. Martina, S. Gherardini, and F. Caruso, Machine learning classification of non-markovian noise disturbing quantum dynamics, *Physica Scripta* **98**, 035104 (2023).
- [35] E. Canonici, S. Martina, R. Mengoni, D. Ottaviani, and F. Caruso, Machine learning based noise characterization and correction on neutral atoms nirq devices, *Advanced Quantum Technologies* **7**, 2300192 (2024), <https://onlinelibrary.wiley.com/doi/pdf/10.1002/qute.202300192>.
- [36] N. Dalla Pozza, L. Buffoni, S. Martina, and F. Caruso, Quantum reinforcement learning: the maze problem, *Quantum Machine Intelligence* **4**, 11 (2022).
- [37] S. Das, J. Zhang, S. Martina, D. Suter, and F. Caruso, Quantum pattern recognition on real quantum processing units, *Quantum Machine Intelligence* **5**, 16 (2023).
- [38] M. Parigi, S. Martina, and F. Caruso, Quantum-noise-driven generative diffusion models, *Advanced Quantum Technologies* **n/a**, 2300401 (2024), <https://onlinelibrary.wiley.com/doi/pdf/10.1002/qute.202300401>.
- [39] D. P. Kingma and J. Ba, Adam: A method for stochastic optimization, arXiv:1412.6980 (2014).
- [40] R. Liaw, E. Liang, R. Nishihara, P. Moritz, J. E. Gonzalez, and I. Stoica, Tune: A Research Platform for Distributed Model Selection and Training, arXiv:1807.05118

- (2018).
- [41] P. Baldi and P. J. Sadowski, Understanding dropout, in *Advances in Neural Information Processing Systems*, Vol. 26, edited by C. Burges, L. Bottou, M. Welling, Z. Ghahramani, and K. Weinberger (Curran Associates, Inc., 2013).
 - [42] J. Bergstra, D. Yamins, and D. Cox, Making a science of model search: Hyperparameter optimization in hundreds of dimensions for vision architectures, in *Proceedings of the 30th International Conference on Machine Learning*, Proceedings of Machine Learning Research, Vol. 28, edited by S. Dasgupta and D. McAllester (PMLR, Atlanta, Georgia, USA, 2013) pp. 115–123.
 - [43] J. Bergstra, R. Bardenet, Y. Bengio, and B. Kégl, Algorithms for hyper-parameter optimization, *Advances in neural information processing systems* **24** (2011).
 - [44] L. Li, K. Jamieson, A. Rostamizadeh, E. Gonina, J. Bentzur, M. Hardt, B. Recht, and A. Talwalkar, A system for massively parallel hyperparameter tuning, in *Proceedings of Machine Learning and Systems*, Vol. 2, edited by I. Dhillon, D. Papailiopoulos, and V. Sze (2020) pp. 230–246.

SUPPLEMENTARY MATERIAL

Fig. S1a reports the normalized error for the raster scans of different simulated datasets and at different subsampling levels. The blue dots are calculated on 2 000 samples that were subsampled to the specified number of measurements and then linearly interpolated to the full size of 600 points. The red points are generated similarly with the exception that the samples are filtered to always have eight deeps without overlapping. In that case, the error is understandably lower. Finally, the purple squares are the normalized errors for 10 000 not interpolated samples.

Fig. S1b is equivalent to Fig. S1a but reports the MAE of the trained ML models. For the blue and red points the samples with less than 600 measurement points were linearly interpolated to the full size. Thus, in those cases we trained a single model with the full raster scan, and we tested it with the interpolated data. The purple squares represent the results of the models trained directly on the subsampled data. Thus for every point of the curve, a different model was trained and tested. The models used for the red points in Fig. S1b are trained with the same data used for the red points of Fig. S1a. Also in this case the error using the filtered data is understandably lower respect to the one that presents overlapping Lorentzians. However, it is remarkable that there is only a slightly difference between the two cases and that the ML models, contrarily to the raster scan, performs well also with the unfiltered data.

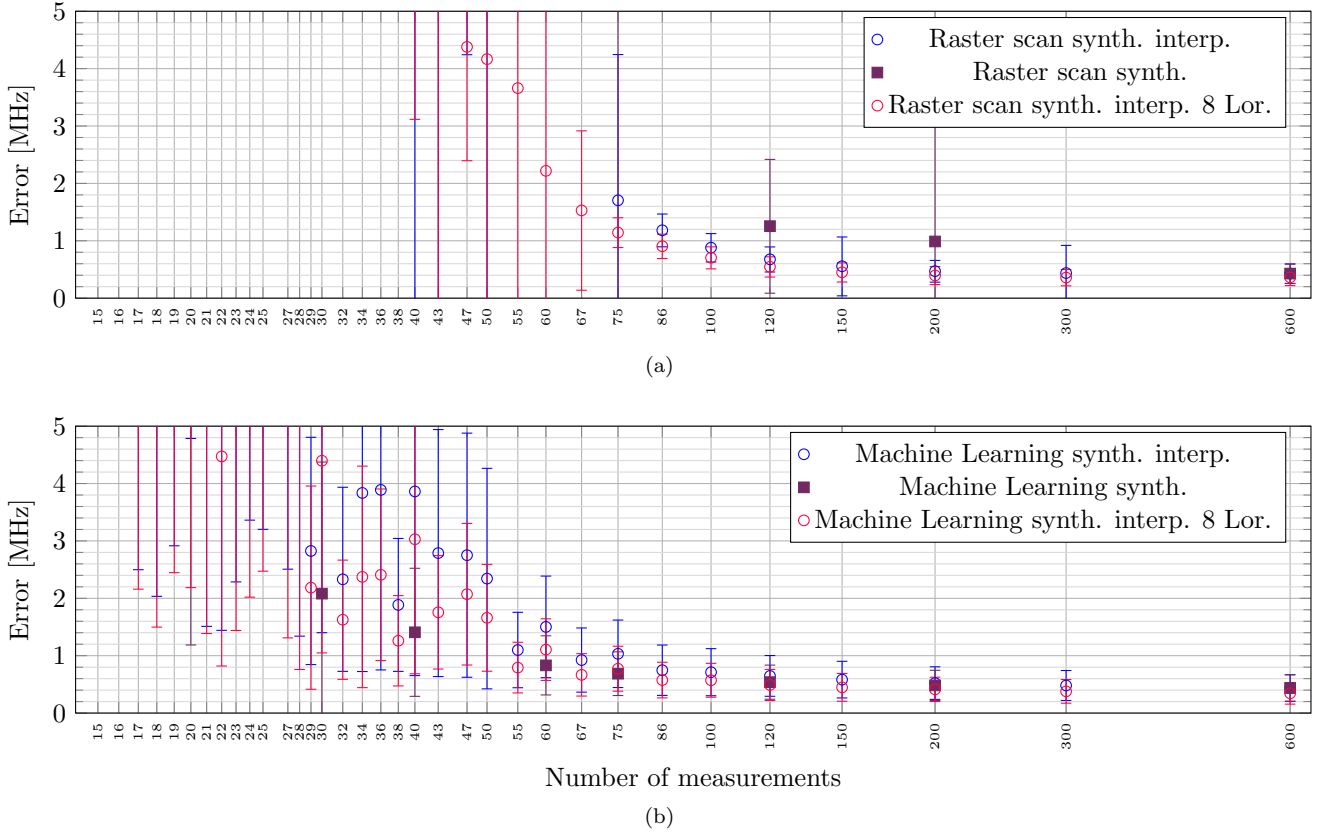


FIG. S1. (a) Normalised mean error of subsampled raster scans: blue circles show the error for 2 000 synthetic interpolated samples (the same of Fig. 2b in the main text). In purple squares, the same 2 000 synthetic samples that were subsampled but not interpolated. The red plot is similar to the blue, however all data samples are filtered to display eight non-overlapping Lorentzians. (b) MAE of ML networks: in Purple squares, networks were trained on 10 000 synthetic samples, and validated with 2 000 synthetic samples. In the latter, the networks were trained for specific number of data points (trained on subsampled datasets), i.e, each point on the graph depicts the result of a different network. The blue circles depict the result of one network, that was trained with 10 000 synthetic samples, and validated with 2 000 synthetic samples, all at full length with 600 measurement points (the same of Fig. 2b in the main text). The subsampled test data was linearly interpolated to the full length (600 points) before using the network to get the predictions. The red plot is similar to the blue, however it was trained on a dataset in which all data samples displayed eight non-overlapping Lorentzians.